Journal of the Optical Society of America A
OPTICS, IMAGE SCIENCE, AND VISION

Fourier optics modeling of interference microscopes

PETER J. DE GROOT* AND XAVIER COLONNA DE LEGA

Zygo Corporation, Laurel Brook Road, Middlefield, Connecticut 06455, USA
**Corresponding author: peterd@zygo.com*

Received 18 February 2020; revised 7 April 2020; accepted 8 April 2020; posted 8 April 2020 (Doc. ID 390746); published 30 April 2020

We propose a practical theoretical model of an interference microscope that includes the imaging properties of optical systems with partially coherent illumination. We show that the effects on measured topography of a spatially extended, monochromatic light source at low numerical apertures can be approximated in a simplified model that assumes spatially coherent light and a linear, locally shift-invariant transfer function that accounts for optical aberrations and the attenuation of diffracted plane wave amplitudes with increasing spatial frequencies. Simulation of instrument response using this model agrees with methods using numerical pupil-plane integration and with an experimental measurement of surface topography.

https://doi.org/10.1364/JOSAA.390746

1. INTRODUCTION

Surface-topography measuring interferometers are widely used in research and production quality control. Laser Fizeau interferometers measure prisms, spheres, and optical flats up to a meter in diameter [1], while interference microscopes reveal surface details on lateral scales below a micrometer [2]. Modern systems measure microlenses [3], automotive components [4], transparent films [5,6], crystallographic surface structures [7], and additively manufactured parts [8,9]. It is of interest to analyze the response of these systems with the goals of improved reliability, accuracy, robustness, and range of application.

Although interferometers are well established in practice, the fundamental measurement principle of these instruments remains a topic of active research. Interferometers for full-field surface-topography measurement rely on imaging optics, with the interference effect providing sensitivity to surface height information. There have been extensive efforts to model interferometer response based on imaging theory to characterize the lateral resolution and spatial frequency response [10–13]. Researchers have evaluated interferometer linearity [14,15] as well as the effects of aberrations and lateral camera sampling [16]. Standardization of instrument specifications has identified fundamental metrological characteristics and calibration methods based on instrument models [17–19].

Modeling methods for interferometers routinely employ scalar diffraction and the concept of an angular spectrum of plane waves. This is solidly in the tradition of Goodman's celebrated textbook [20] as well as many other basic treatments of Fourier optics [21,22]. An essential first step in this approach is the definition of what Frieden refers to as a *transverse* object, equivalent to an aperture function with a phase distribution that is confined to a plane normal to the optical axis [23]. The concept derives historically from the visual observation of interference patterns with fringes that occur at intervals that are proportional to surface height [24]. Fourier analysis of the frequency content of this 2D distribution enables a calculation of the propagating light field and the filtering effects of apertures in the optical system. In this paper, models that rely on a 2D representation of fields and surfaces are referred to collectively as the *elementary Fourier optics* (EFO) method.

The modeling of what is fundamentally a 3D problem using a 2D grid implicitly assumes that all surface points can be at the same focus position at the same time. While this is nearly true for large-aperture, coherent laser Fizeau interferometers, it is a less satisfying approximation for interference microscopy, when the sharpness and contrast of interference fringes can vary over the surface topography. Given these limitations, 3D Fourier optics methods have played an increasing role in modeling holography, confocal microscopy, and quantitative imaging [23,25,26]. Coupland and colleagues have developed 3D transfer functions for holography and interferometry of reflecting surfaces based on the concept of scattering from an infinitesimally thin layer representing the height distribution in 3D [27,28]. In addition to these advances, there has been extensive work in surface scattering theory using rigorous coupled wave analysis [29] and boundary element methods [30].

The benefits of 3D modeling and rigorous diffraction analysis notwithstanding, the more basic EFO method together with classical Abbe theory continues to play an important role in understanding how interferometers work [14,31]. A 2D complex-valued representation of the surface is adequate for many measurement configurations where the topography

variations are within the depth of field. EFO methods are straightforward to implement using computationally efficient fast Fourier transforms [22], and are useful in understanding how physical apertures and aberrations influence spatial frequency response [14]. Therefore, somewhat contrary to current trends that strive to improve diffraction calculations on difficult surface structures, the goal of the present paper is to provide the simplest possible interferometer model that realistically includes the imaging properties of the optical system. A specific case of interest here is interferometry with partially coherent light, which is common in reflection interference microscopes for surface-topography measurement. While modeling of partially coherent systems can be quite complex, we show that a significant simplification follows from using familiar approximations such as an obliquity factor for fringe spacing.

This paper is structured as follows. Section 2 describes a generic interference microscope, followed by an EFO model for monochromatic coherent imaging with a single source point. The theory extends to partially coherent light with diffuse light sources using a pupil integration method. It is then shown that with specific approximations, the pupil integration reduces to a simple procedure that parallels the coherent case, but with a transfer function that accounts for the gradual attenuation of the plane wave spectrum at increasing spatial frequencies. Finally, we apply this approximate EFO model to the task of determining instrument response to sinusoidal surface features, to illustrate how optical filtering influences the topographical lateral resolution of interferometers.

2. THEORY

A. Instrument Model

Figure 1 shows a digital interference microscope with a monochromatic Köhler illuminator, an electronic camera, and computerized data processing to convert interference fringe information to surface heights [2].

The objective lens in Fig. 1 has a numerical aperture (NA) determined by its focal length and the objective aperture stop positioned at the back focal plane of the objective. The objective stop is the limiting aperture for the imaging pupil and restricts the range of scattered ray angles from the object surface that may be captured by the imaging system. The maximum inclination angle for an NA A_N and a refractive index equal to 1 is

$$\beta = \sin^{-1}(A_N). \tag{1}$$

In EFO modeling, the basic assumption is that variations in surface height are small when compared to the depth of field given by the Rayleigh formula

$$D_{\text{field}} = \pm\lambda/A_N^2. \tag{2}$$

For a wavelength of 0.50 μm, the depth of field typically ranges from ±100 μm at 0.05 NA to ±1 μm at 0.5 NA.

In an epi microscope with an extended light source, the objective aperture stop is often the limiting aperture for the illumination. However, by adjusting the aperture stop for the source, it is possible to underfill the objective aperture. For a point-like monochromatic light source such as a laser or a very small aperture stop, the illumination is spatially coherent, whereas if the light source is diffuse and its image fills the objective aperture, the illumination is partially coherent, approaching fully incoherent at high NA.

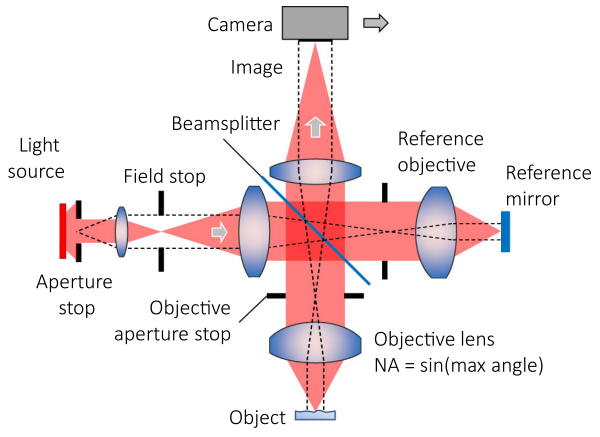

Fig. 1. Conceptual diagram for an interference microscope.

B. Interferometry with Coherent Illumination

Referring to Fig. 2, the object-space geometry has a z axis defined by the optical axis of the instrument and a lateral x, y coordinate plane at a position $z = 0$ positioned at the average surface height when the object is in focus. In the equations that follow, we show a single lateral coordinate x to simplify the notation. The extension to a 2D lateral coordinate system is straightforward with the addition of the y axis, directed orthogonally inwards to the plane of Fig. 2.

In the coherent EFO model, a light source of wavelength λ and unit intensity illuminates an object surface with a single plane wave propagating downward along the z axis and having an angular wavenumber

$$k = 2\pi/\lambda. \tag{3}$$

In EFO modeling, the effect of topography is to introduce phase shifts proportional to surface heights $h_o(x)$:

$$\theta_o(x) = 2kh_o(x). \tag{4}$$

Immediately after reflection, we have a complex scalar object light field distribution $U_o(x)$ within a plane at $z = 0$ that represents the object surface:

$$U_o(x) = \exp[-i\theta_o(x)], \tag{5}$$

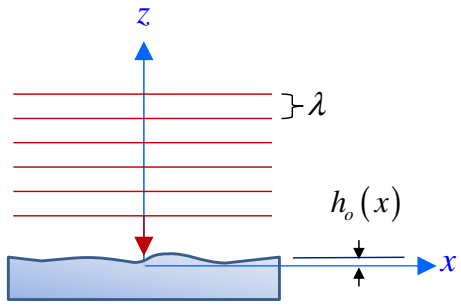

Fig. 2. Coherent plane wave illumination at normal incidence to the object surface.

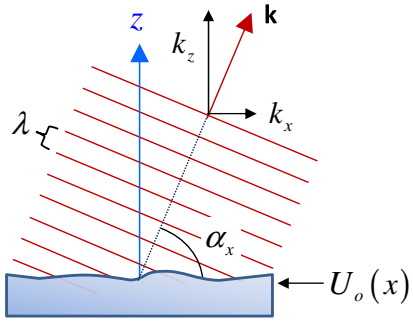

Fig. 3. Diffracted plane wave component of the object light field distribution.

where the intensity (or irradiance) for the reflected light field is normalized to one over the full field of view. In addition to the 2D representation of surfaces and light fields, EFO modeling implicitly neglects multiple scattering, and assumes that local surface curvatures are small enough to be consistent with the Kirchhoff approximation [32]. Although Fresnel reflections, polarization effects, and skew angles can be included in EFO methods [33], here we are only concerned with surface geometry in a simple cross-sectional model and will neglect these effects.

Consistent with classical Fourier optics methods, the diffracted object light field is equivalent to a linear sum of non-evanescent plane waves, each of which satisfies the Helmholtz equation for free-space propagation [20,34]. Referring now to Fig. 3, each diffracted plane wave has the form

$$\rho(x, z) = \exp[i(k_x x + k_z z)], \tag{6}$$

where k_x, k_z are the projections of a vector $\mathbf{k}$ of length k aligned with the propagation direction of the plane wave. We can also write the wavenumbers in terms of spatial frequencies:

$$k_x = 2\pi f_x. \tag{7}$$

The propagation angle in terms of this lateral spatial frequency is given by

$$\cos(\alpha_x) = k_x/k = \lambda f_x. \tag{8}$$

The spectrum of plane waves at $z = 0$ is the forward Fourier transform of the object light field over the coordinate x:

$$\widetilde{U_o}(f_x) = \int U_o(x) \exp(-i2\pi f_x x)\mathrm{d}x, \tag{9}$$

which we will write as

$$\widetilde{U_o}(f_x) = \mathcal{F}\{U_o(x)\}. \tag{10}$$

The tilde ($\sim$) symbol denotes a frequency-domain representation of the corresponding space-domain quantity. For an optical system that obeys the Abbe sine condition [35], the reflected plane wave spectrum is physically realized at the back focal plane of the objective. The sine condition is satisfied generally in the far field by a paraxial approximation, and is a design goal of most microscope objectives, even at high NA.

If the object surface is not at the best focus position, we use a free-space propagator

$$\wp(f_x, z) = \exp\left[ikz\sqrt{1 - (\lambda f_x)^2}\right] \tag{11}$$

to account for how much each plane wave will be shifted in phase in terms of the propagation distance [22]:

$$\widetilde{U_o}(f_x, z) = \wp(f_x, z)\widetilde{U_o}(f_x). \tag{12}$$

The square root in the propagator implies that we retain only those non-evanescent plane waves for which $\lambda f_x \le 1$. The inverse Fourier transform provides the resulting light field from the focus-shifted spectrum of plane waves:

$$U_o(x, z) = \mathcal{F}^{-1}\left\{\widetilde{U_o}(f_x, z)\right\}$$
$$= \int \widetilde{U_o}(f_x, z) \exp(i2\pi f_x x)\mathrm{d}f_x. \tag{13}$$

This calculation is useful for showing how the light field propagates after reflection, as well as for determining and potentially correcting the effects of defocus [36].

The modeling of image formation includes the filtering properties of the optical system. Following classical results for coherent illumination, this filtering is a linear shift-invariant process in complex amplitude, characterized by an amplitude transfer function (ATF) [20]. The effect on the spectrum of plane waves is a multiplication in frequency space

$$\widetilde{U_I}(f_x, z) = \widetilde{H}(f_x)\widetilde{U_o}(f_x, z), \tag{14}$$

where $\tilde{H}$ is the complex-valued ATF. For the geometry of Fig. 1, the objective aperture limits the bandwidth of the ATF to spatial frequencies $|f_x|$ that are no larger than

$$f_N = A_N/\lambda. \tag{15}$$

In real systems with optical aberrations and transmission efficiencies that depend on ray angles, there are magnitude and phase terms in the ATF within the bandwidth limits.

At the image plane, the coherent superposition of the filtered plane waves results in an imaged light field given by the inverse Fourier transform

$$U_I(x, z) = \mathcal{F}^{-1}\left\{\widetilde{U_I}(f_x, z)\right\}. \tag{16}$$

In principle, the image coordinates should include the magnification, the image inversion, and possibly even the distortion in the coordinate mapping. For the present purpose, it is convenient to reuse the object-space coordinates x, z. The calculation of the topography follows from a determination of the phase of the imaged light field, ideally at the best focus position:

$$\theta_I(x) = -\arg\{U_I(x)\}. \tag{17}$$

The topography measurement is

$$h_I(x) = \theta_I(x)/2k = \lambda\theta_I(x)/4\pi. \tag{18}$$

Because the phase range covers only 2π, the measured value should be unwrapped or connected to cover the full topography range [37].

In practice, determining the phase interferometrically may proceed by any one of a number of ways, for example, by mixing the imaged light field with the reference field and performing

phase shifts to generate a signal for further processing [38]. However, for the purposes of mathematically modeling the optical filtering effects on the measured surface topography, it is enough to calculate the phase directly from Eq. (17).

C. Partially Coherent Illumination—Pupil-Plane Integration

A common microscope configuration is an incandescent lamp or light-emitting diode imaged into the illumination pupil [39]. The distribution of source points within the pupil results in a range of incident angles as viewed by the object. Even with the assumption that the light source is spatially incoherent, the imaging process is best described as partially coherent. Modeling the system involves integrating over source points in the illumination pupil [22,40,41]. Here we describe how such a calculation applies to an EFO model of an interferometer.

The first step in the calculation is to determine the interference intensity pattern for just one plane wave corresponding to a single source point in the illumination pupil. Figure 4 shows a plane wave of the form

$$\rho^o(x, z) = \tilde{p}(f_x^o)\exp[i(k_x^o x + k_z^o z)], \tag{19}$$

where the superscript "o" is for the incident wave, $\tilde{p}$ is the normalized real-valued pupil-plane magnitude distribution, and

$$f_x^o = k_x^o/2\pi. \tag{20}$$

From the figure, a positive value of f_x^o corresponds to a source point originating on the left-hand side of the optical axis. If a perfectly flat mirror were placed at the x, y plane, this wave would reflect upwards at the angle α_x^o shown in Fig. 4, given by

$$\cos(\alpha_x^o) = \lambda f_x^o. \tag{21}$$

If the source light is limited by the objective aperture stop, the magnitude distribution $\tilde{p}$ is limited to a maximum frequency f_N determined by the NA, as in Eq. (15).

The sensitivity of the reflected light field phase to surface heights is proportional to the wavevector projection along the z axis according to

$$\theta_o(x, f_x^o) = 2kh_o(x)\sin\left[\alpha_x^o(f_x^o)\right]. \tag{22}$$

Setting aside for the moment the weighting factor $\tilde{p}$ and assuming that the surface reflectivity has no angular dependence, the reflected light field for a single source point from the extended light source is

$$u_o'(x, f_x^o) = u_o(x, f_x^o)\exp\left(i2\pi f_x^o x\right), \tag{23}$$

where

$$u_o(x, f_x^o) = \exp[-i\theta_o(x, f_x^o)], \tag{24}$$

and the phase factor $2\pi f_x^o x$ in the primed variable u_o' accounts for the added phase shift along the x axis resulting from the inclination of the incident beam. Using the Fourier shift theorem, the resulting spectrum of plane waves can be expressed as

$$\tilde{u}_o'(f_x, f_x^o) = \tilde{u}_o(f_x - f_x^o, f_x^o), \tag{25}$$

which corresponds to a frequency shift f_x^o for a plane wave spectrum given by

$$\tilde{u}_o(f_x, f_x^o) = \mathcal{F}\{u_o(x, f_x^o)\}. \tag{26}$$

Physically, the frequency difference $f_x - f_x^o$ can be visualized by noting that the angles α_x, α_x^0 in Fig. 4 are related by

$$\lambda(f_x - f_x^o) = \cos(\alpha_x) - \cos(\alpha_x^o). \tag{27}$$

The ATF $\tilde{H}$ in Eq. (14) describes the optical filtering of the shifted spectrum of plane waves u_o'. In terms of the unshifted spectrum $\tilde{u}_o$, the filtered image spectrum is

$$\tilde{u}_I(f_x, f_x^o) = \tilde{H}(f_x + f_x^o)\tilde{u}_o(f_x, f_x^o). \tag{28}$$

Equation (28) resembles diffraction with a single normal-incidence plane wave with an ATF that shifts laterally with f_x^o. This is the well-known effect that illuminating plane waves over a range of oblique incident angles broadens the spatial frequency response to surface structures [42,43]. The final imaged light field at the camera is

$$u_I'(x, f_x^o) = \mathcal{F}^{-1}\left\{\tilde{u}_I(f_x - f_x^o, f_x^o)\right\}, \tag{29}$$

which from the Fourier shift theorem is

$$u_I'(x, f_x^o) = u_I(x, f_x^o)\exp(i2\pi f_x^o x), \tag{30}$$

where

$$u_I(x, f_x^o) = \mathcal{F}^{-1}\left\{\tilde{u}_I(f_x, f_x^o)\right\}. \tag{31}$$

Similarly to the coherent case, the propagator given in Eq. (11) applied to the spectrum of plane waves accounts for the object surface being out of focus.

In an interferometer with an extended, incoherent source, the imaged light field is superimposed coherently with a reference plane wave originating from the same point in the illumination pupil and imaged through the optical system after reflection from a flat, uniformly reflecting reference surface. If we assume a common reference phase θ_R over the full field of view and unit reflectivity and again setting aside for the moment the weighting factor $\tilde{p}$, the in-focus reference light field just after reflection from a perfectly flat mirror is

$$u_{Ro}'(x, f_x^o) = \exp(-i\theta_R)\exp(i2\pi f_x^o x). \tag{32}$$

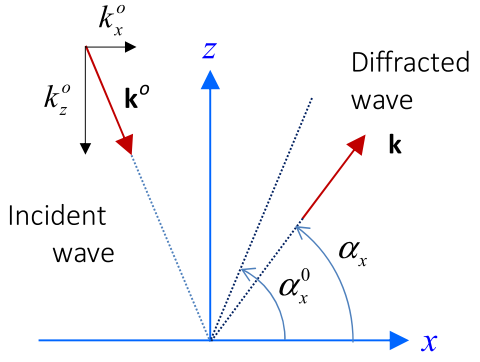

Fig. 4. Geometry for a single off-axis incident plane wave and a diffracted plane wave.

There is no diffraction for a flat reference mirror other than specular reflection; therefore $f_x = f_x^o$ and the imaged reference field after filtering by the ATF simplifies to

$$u'_R(x, f_x^o) = \tilde{H}(f_x^o)\exp(i\theta_R)\exp(i2\pi f_x^o x). \tag{33}$$

After mixing the imaged object and reference light fields on a square-law detector, the measured interference signal for this source contribution is

$$\varsigma(x, f_x^o) = \left|u'_I(x, f_x^o) + u'_R(x, f_x^o)\right|^2. \tag{34}$$

Hiding for a moment some of the dependencies for compactness, the interference intensity pattern contribution for this source point is

$$\varsigma(x, f_x^o) = \left|u'_R\right|^2 + \left|u'_I\right|^2 + u'_I u'^*_R + u'^*_I u'_R. \tag{35}$$

We will have a look at each term in sequence.

The most straightforward term in Eq. (35) is the contribution from the reference to the interference intensity, which, as defined here, is independent of field position, reference phase, and object surface topography:

$$\left|u'_R\right|^2 = \left|\tilde{H}(f_x^o)\right|^2. \tag{36}$$

The next term is also a real value and is independent of the reference phase:

$$|u'_I|^2 = \left|u_I(x, f_x^o)\right|^2. \tag{37}$$

The third term in Eq. (35) relates to the interference between the reference and object reflections:

$$u'_I u'^*_R = \exp(i\theta_R)\widetilde{H}^*(f_x^o)u_I(x, f_x^o). \tag{38}$$

It is noteworthy that for all of the terms in Eq. (35), the inclination phase factor $2\pi f_x^o x$ no longer appears and we can use the unprimed light field component variable u_I.

To determine the total interference signal as viewed by the camera, the weighted sum of all the contributions ς over the illumination pupil results in a signal

$$\Upsilon = \Upsilon_R + \Upsilon_I + \Upsilon_{IR} + \Upsilon^*_{IR}. \tag{39}$$

The first two offset terms are

$$\Upsilon_R = \int \tilde{P}(f_x^o)|\tilde{H}(f_x^o)|^2 \mathrm{d}f_x^o \tag{40}$$

and

$$\Upsilon_I = \int \tilde{P}(f_x^o)|u_I(x, f_x^o)|^2 \mathrm{d}f_x^o, \tag{41}$$

where

$$\tilde{P}(f_x^o) = \left[\tilde{p}(f_x^o)\right]^2 \tag{42}$$

is the intensity distribution in the illumination pupil. The interference term is

$$\Upsilon_{IR} = \mathrm{U}^*_R \mathrm{U}_I, \tag{43}$$

where by definition

$$\mathrm{U}^*_R = \exp(-i\theta_R) \tag{44}$$

and

$$\mathrm{U}_I(x) = \int \tilde{P}(f_x^o)\widetilde{H}^*(f_x^o)u_I(x, f_x^o)\mathrm{d}f_x^o. \tag{45}$$

The interference fringes are given by

$$\mathrm{Re}\{\Upsilon_{IR}\} = |\Upsilon_{IR}|\cos(\theta_I - \theta_R) \tag{46}$$

for

$$\theta_I(x) = -\arg\{\mathrm{U}_I(x)\}. \tag{47}$$

The non-italicized variable U_I is analogous to a light field, and we will refer to it as such, but it is more accurately described as the complex representation of the object-dependent contribution to the modulating portion of the interference signal Υ_{IR}. In fully coherent illumination, U_I is the same as the light field variable U_I.

The pupil-plane integration can account for incident-angle variations in surface reflectivity, phase change on reflection, and diffraction efficiency [41,44]. However, in a realistic instrument model, Eq. (45) would involve nested integrals over the two x, y lateral dimensions. In addition to being computationally intensive, it is difficult to interpret the pupil-plane integration in terms of familiar transfer functions for optical imaging. In the next section, we shall show that the use of approximations familiar to classical interference microscopy leads to a significant simplification of the calculation of the interference fringe signal.

D. Approximate EFO Model Using an Equivalent Wavelength

Starting with Eq. (45) for the object contribution to the interference pattern and expanding the contribution u_I, we have

$$\mathrm{U}_I(x) = \int \tilde{P}(f_x^o)\widetilde{H}^*(f_x^o)\left[\int \tilde{H}(f_x + f_x^o)\widetilde{u_o}(f_x, f_x^o) \times \exp(i2\pi f_x x)\mathrm{d}f_x\right]\mathrm{d}f_x^o. \tag{48}$$

By approximating the effect of multiple incident angles with the average effect at a single averaged inclination angle for the reflected object field contributions u_o, the dependence of $\widetilde{u_o}$ on the pupil frequency f_x^o shown in Eq. (22) is removed, enabling the following separation of variables:

$$\mathrm{U}_I(x) \approx \int \left[\int \tilde{P}(f_x^o)\widetilde{H}^*(f_x^o)\tilde{H}(f_x + f_x^o)\mathrm{d}f_x^o\right]\widetilde{u_o}(f_x) \times \exp(i2\pi f_x x)\,\mathrm{d}f_x. \tag{49}$$

This is the same as

$$\mathrm{U}_I(x) = \mathcal{F}^{-1}\{\tilde{O}(f_x)\widetilde{\mathrm{U}}_o(f_x)\}, \tag{50}$$

where the integration over f_x^o in Eq. (49) is recognized as a cross correlation [45]:

$$\tilde{O}(f_x) = \left[\tilde{P}(f_x)\tilde{H}(f_x)\right] \star \tilde{H}(f_x). \tag{51}$$

The quantity $\tilde{O}(f_x)$ is the approximate transfer function for interference fringes in partially coherent light, abbreviated here as PCTF. The complex representation of the object contribution to the interference signal is then

$$\widetilde{\mathrm{U}}_o(f_x) = \mathcal{F}\{\mathrm{U}_o(x)\}. \tag{52}$$

The contribution of the object surface to the interference fringes is

$$\mathrm{U}_o(x) = \exp[-i\theta_{\mathrm{eq}}(x)] \tag{53}$$

for an incident-angle independent phase distribution

$$\theta_{\mathrm{eq}}(x) = 2k_{\mathrm{eq}}h_o(x) \tag{54}$$

that depends on an *equivalent wavenumber* k_{eq} and an associated *obliquity factor* defined by

$$\Omega = k/k_{\mathrm{eq}}. \tag{55}$$

The rescaling of the wavenumber also applies to the interpretation of the interference phase

$$h_I(x) = \theta_I(x)/2k_{\mathrm{eq}}. \tag{56}$$

This scaling accounts for the increased spacing of interference fringes at oblique incidence.

The use of an obliquity factor to correct for the effect of a converging cone of illumination is well known in interference microscopy [2,46,47]. There are several approaches to calculating its value, with most equivalent to averaging the z-axis component of the vector $\mathbf{k}$ over all the positions within the boundaries of a circular illumination pupil. A well-known approximate solution for low NA is

$$\Omega = 2/[1 + \cos(\beta)], \tag{57}$$

where the angle β is defined by Eq. (1) for a filled illumination pupil, or, alternatively, by the size of the source image in the pupil. Another approach is to determine the equivalent wavenumber empirically as part of a measurement sequence, by scanning the object axially at a known displacement rate and detecting the interference fringe frequency [48].

To use an equivalent wavelength, the object should be near the best focus position. As the object moves away from this position, or if the surface heights become significant compared to the depth of field, the effect of defocus is a loss of contrast for the interference fringes caused by the angular dependence of the phase shifts of the component incident beams with z position. However, it is possible to at least partially extend the useful focus range for the approximation using a closed-form fringe contrast function as an overall multiplicative factor [46,49]. The effect of defocus on the image sharpness can also be accommodated in the same way as the coherent case, by applying the propagator defined in Eq. (10) to the spectrum of plane waves.

For the case of a uniformly filled illumination pupil, the PCTF defined in Eq. (51) takes on the form of the incoherent optical transfer function (OTF)

$$\tilde{O}(f_x) = \tilde{H}(f_x) \star \tilde{H}(f_x). \tag{58}$$

The modulus of the OTF is the familiar magnitude transfer function (MTF) for conventional imaging [20,50]. The inverse Fourier transform of the OTF is the incoherent point spread function (PSF)

$$O(x) = |H(x)|^2. \tag{59}$$

A well-known example OTF is given by the autocorrelation of a 2D circular pupil [20], which works out to

$$\tilde{O}(f_x) = \frac{2}{\pi}\left[\cos^{-1}\left(\frac{|f_x|}{f_{\max}}\right) - \frac{|f_x|}{f_{\max}}\sqrt{1-\left(\frac{|f_x|}{f_{\max}}\right)^2}\right] \times \mathrm{rect}\left\{\frac{f_x}{2f_{\max}}\right\}, \tag{60}$$

where the maximum detectable lateral spatial frequency is twice that of Eq. (15):

$$f_{\max} = 2f_N = 2A_N/\lambda. \tag{61}$$

The higher spatial frequency limit is often cited as an advantage of a spatially extended source. Note that in Eq. (60), the variable f_x is equivalent to a radial coordinate for the circular pupil. Table 1 summarizes this approximate EFO procedure for interference microscopy in partially coherent light using the obliquity-factor approximation.

The example of a uniformly filled illumination pupil allows for useful intuitive interpretation of interferometry. If we imagine the interference fringes as having been formed at the object surface, then imaging these intensity fringes will involve the incoherent OTF [27]. This concept should be used with caution, given that this is not actually what is happening physically—the illumination is only partially coherent, and square-law detection and time averaging take place at the camera. To appreciate the difference, we need look no further than the intensity offset Υ_I. Using the same obliquity-factor approximation, Eq. (41) becomes

$$\Upsilon_I = \int \tilde{P}(f_x^o) \times \left|\int \tilde{H}(f_x + f_x^o)\widetilde{u_o}(f_x)\exp(i2\pi f_x x)\mathrm{d}f_x\right|^2 \mathrm{d}f_x^o. \tag{62}$$

This equation cannot be simplified in general to a form that makes use of the traditional incoherent OTF. Further, the detected average intensity in Eq. (62) has a surface slope dependence that would not be present if the conversion to interference intensity took place at the surface, rather than at the camera [51–53].

3. APPLICATION: THE INSTRUMENT TRANSFER FUNCTION

A. Definition and Evaluation of the ITF

The EFO has several uses; one of the most important is to predict the instrument response to various surface structures. The instrument transfer function (ITF) quantifies the height response as a function of the spatial frequency of the surface topography, under the assumption that the response is at least

Table 1. Approximate EFO Model for Partially Coherent Light

Step	Symbols	References
Determine the obliquity factor and equivalent wavenumber based on the light distribution in the illumination pupil	Ω, k_{eq}	Eq. (3), Eq. (57)
Define an object topography and equivalent phase for the object light field after reflection from the surface	h_o, θ_{eq}	Eq. (4), Eq. (55)
Calculate the complex representation of the object light field and use a Fourier transform to obtain the spectrum of plane waves	$\mathrm{U}_o, \tilde{\mathrm{U}}_o$	Eq. (53), Eq. (52)
Define the light intensity distribution in the illumination pupil and the ATF for the imaging optics	$\tilde{P}, \tilde{H}$	Eq. (42), Eq. (15)
Calculate the PCTF	$\tilde{O}$	Eq. (51)
Filter the spectrum of plane waves using the PCTF, and calculate the imaged light field using an inverse Fourier transform	$\tilde{\mathrm{U}}_I, \mathrm{U}_I$	Eq. (50)
Calculate the measured phase and corresponding surface heights	θ_I, h_I	Eq. (56)

approximately linear [13,17]. A common definition for the ITF is the square root of the ratio of the power spectral density (PSD) of the measured topography to the known object topography at each surface spatial frequency ν:

$$T(\nu) = \sqrt{\mathrm{PSD}_I(\nu)/\mathrm{PSD}_o(\nu)}, \tag{63}$$

where the PSD is given by the square magnitude of the Fourier components of the surface topography [54,55]. Here we assume that ITF contributions such as camera sampling and electronic filtering are either negligible or not of interest when evaluating the optical system.

An evaluation of the ITF using optical models involves presenting a simulated instrument with a sequence of sinusoidal patterns and recording the results [13,16,31]. Each of these patterns has the form

$$h_o(\nu, x) = b_o \sin(2\pi \nu x) \tag{64}$$

for a real-valued surface amplitude b_o. After simulating the corresponding output profile h_I, the measured amplitudes are

$$b_I(\nu) = \int h_I(\nu, x) \exp(i2\pi \nu x)\mathrm{d}x, \tag{65}$$

with appropriate normalizations so that the ITF may be calculated directly from

$$T(\nu) = |b_I(\nu)/b_o|. \tag{66}$$

Note that the value of b_I as calculated from Eq. (65) can in principle be complex, if there is a lateral shift in the position of the sample sinusoid.

B. ITF in the Limit of Small Surface Heights

For small surface height variations, it is known that the ITF corresponds closely to the transfer function for the optical imaging system, assuming that there are no other significant contributions such as sparse camera sampling [31,56]. The small-height approximation for Eq. (53) with the approximate EFO model is

$$\mathrm{U}_o(x) \approx 1 + 2ik_{\text{eq}}h(x), \tag{67}$$

where the height range is much smaller than the wavelength λ. Applying Eqs. (50)–(56) from Section 2.D, it is straightforward to show that the measured amplitudes are

$$b_I(\nu) \approx \tilde{O}(\nu)b_o, \tag{68}$$

and therefore

$$T(\nu) \approx |\tilde{O}(\nu)|. \tag{69}$$

This result shows that the interferometer ITF will follow the MTF for small-height variations. This has been confirmed experimentally and reported in prior publications [2].

An important aspect of the small surface height limit is that it predicts linear response to sharp surface discontinuities in the surface structure such as step heights. This is not the case in general—a sharp edge or other features that are inconsistent with the Kirchoff approximation can result in significant nonlinear response if they exceed the small-height limit [14].

C. ITF for Fixed Maximum Slope

While the small-height limit described in the previous section is a useful starting point, common applications in interference microscopy and the testing of optical components involve surface height variations that frequently exceed the wavelength. Importantly, there is no fundamental reason why the ITF should have the same mathematical form as the MTF for all surface geometries. It is therefore of interest to perform a simulation of instrument response for sinusoids of larger amplitude. As we shall show here, the interferometer ITF for sinusoidal surface variations has a flatter response over a wide range of surface spatial frequencies than the MTF.

When simulating more varied surface topographies, it is important to consider that surface slopes may be too steep for the reflected light to pass through the optical system, resulting in signal loss [17]. Given the slope limitations for optical systems, when calculating the ITF, it is meaningful to calculate the response with a fixed maximum slope angle instead of a fixed sinusoidal amplitude [57]. The steepest slope angle for a sinusoid is at the zero crossings:

$$s(\nu) = \tan^{-1}(2\pi\nu b_o). \tag{70}$$

For an interference microscope with a source image that fills the objective aperture stop, the geometrical limit based on specular reflection is equal to the acceptance angle β calculated from the NA using Eq. (1). The usual guidance is to have surface slopes well below the geometrical limit, so as to have sufficient signal

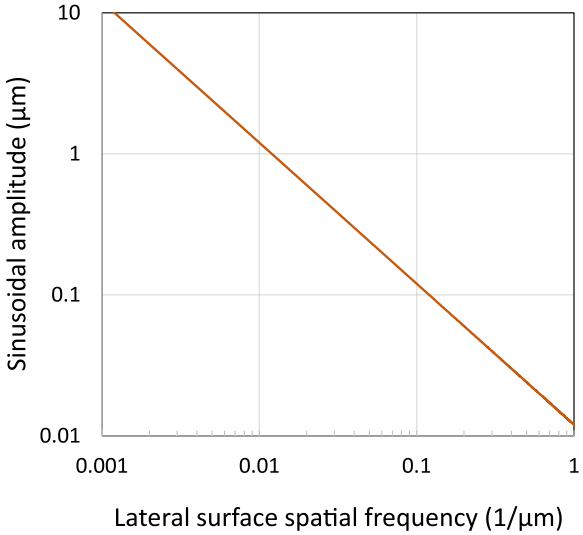

Fig. 5. Amplitude of sinusoidal surface topography as a function of frequency for a fixed maximum slope angle equal to 50% of the acceptance angle for an NA of 0.15.

strength and to capture all of the interference fringe frequencies [14,17]. As an example, setting the surface slope at 50% the geometrical limit, the amplitude as a function of frequency is

$$b_o(\nu) = \tan(\beta/2)/2\pi\nu. \tag{71}$$

Figure 5 illustrates a range of surface heights as a function of frequency for an NA of 0.15. The lateral spatial frequency range extends from a single sinusoid over a 1 mm field of view to a 1 μm spatial period. The amplitude range spans the ±12 μm depth of field at this NA.

Figure 6 shows the results of an ITF simulation using the amplitude range provided in Fig. 5 and the approximate EFO model of Table 1. The response is nearly flat over two decades of frequencies, which is helpful when evaluating the PSD of surfaces. The results are sufficiently different from the small-height limit represented by the MTF curve that we performed the same simulation using an independently developed model with a complete numerical pupil integration for partially coherent light and a more accurate diffraction model as described in [44]. The agreement shown in Fig. 6 gives us confidence that this behavior is characteristic of interference microscopes, as opposed to an artefact of the modeling.

The response for the interferometer ITF is of importance when comparing with other measurement technologies for surface topography. For an experimental demonstration, we chose a Rubert & Co, Ltd., No. 542 specimen with a sinusoidal period of 8 μm and an arithmetical mean deviation *Ra* of 0.060 μm as measured with a stylus instrument [58]. We measured this sample interferometrically with a 5.5× 0.15 NA Michelson objective and an LED-based narrow-bandwidth illuminator, using phase shifting interferometry [48]. The results in Fig. 7 show a measured *Ra* value close to the 0.052 μm value predicted from the stylus result multiplied by the 87% ITF predicted by the approximate EFO model for partially coherent light at this spatial frequency.

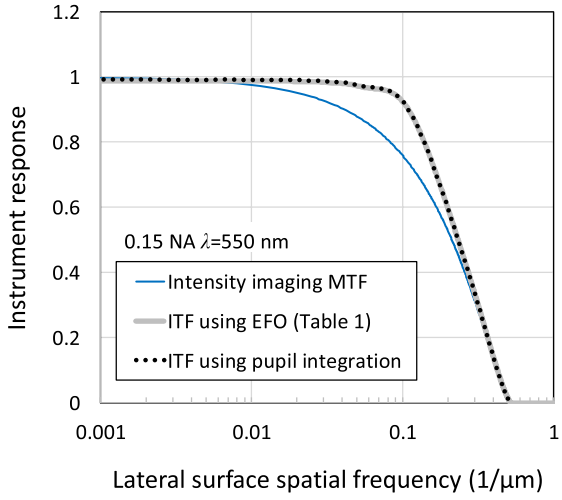

Fig. 6. Simulation of the instrument response for the sinusoidal amplitudes given by Fig. 5.

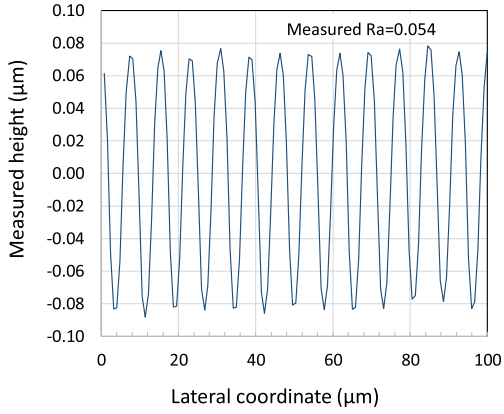

Fig. 7. Interference microscope measurement of surface topography for a sinusoidal specimen, illustrating instrument response at a spatial frequency of 0.125 μm^{-1}.

4. SUMMARY

The physical-optics modeling of interference microscopy can be complicated and computationally intensive. Here we have found that in many cases the basic imaging properties of optical systems can be meaningfully addressed with traditional Fourier optics, using a scattering model that considers the surface as a thin phase grating and a 2D representation of propagating light fields. Within well-recognized limits and with simple surface structures, the model can be useful for predicting interferometer response to sample topography.

In the approximate EFO model summarized in Table 1, a further simplification for partially coherent light follows from the use of the obliquity factor—a familiar concept in interference microscopy that averages the interference phase shift sensitivity over the range of incident angles to the object surface. This simple model neglects angle-dependent reflectivity variations, polarization effects, and skew angles, and assumes that the topography is well within the objective depth of field. With these approximations in place, the interference signal can

be simulated by assuming that the light source is fully coherent, even if it is an extended source such as a monochromatic LED. A linear shift-invariant transfer function—the PCTF—accounts for the optics and the process of forming interference fringes on the camera. The PCTF is the cross correlation of a complex-valued illumination pupil with the coherent imaging ATF. If the source light uniformly fills the objective pupil, the PCTF has the same mathematical form as the familiar OTF for fully incoherent light, even at low NA. Essentially, the instrument is modeled as coherent but with an apodized imaging pupil. This is a much simpler calculation than a formal pupil-plane integration and can leverage 2D fast Fourier transforms.

The approximate EFO model shows that the ITF for monochromatic interference microscopes follows the optical imaging MTF for small surface height variations, but arguably improves as surface heights increase (Fig. 7), provided that we respect the geometrical limits on slope angles imposed by the NA. However, the fact that the ITF is different depending on the surface height variation shows that the ITF is a useful fiction—the response is not perfectly linear in general. This result is not an artifact of the modeling; rather, it is characteristic of interferometry.

The model readily extends to white light interferometry and to coherence scanning, by mathematically superimposing interferometer signals over a range of wavelengths. Although there are clear limitations to such elementary methods, we would argue that many of the most important properties of interferometers, including many basic error mechanisms observed in practice, are within reach of this approach, in spite of its simplicity [14]. In addition, when developing more advanced models, EFO methods are useful for comparison, particularly when elementary methods are proven to be inaccurate, as this indicates situations for which the lateral resolution, linearity, focus effects, and topographical fidelity require a more advanced approach.

Acknowledgment. The authors gratefully acknowledge the contributions and suggestions of Richard Leach, Rong Su, Matthew Thomas, Jeremy Coupland, and Shiguang Wang to this work.

Disclosures. The authors declare no conflicts of interest.

REFERENCES

1. L. L. Deck and J. A. Soobitsky, "Phase-shifting via wavelength tuning in very large aperture interferometers," Proc. SPIE **3782**, 432–442 (1999).
2. P. J. de Groot, "Interference microscopy for surface structure analysis," in *Handbook of Optical Metrology*, T. Yoshizawa, ed. (CRC Press, 2015), pp. 791–828.
3. X. M. Colonna de Lega, M. F. Fay, and P. de Groot, "Optical evaluation of lenses and lens molds," U.S. patent 9,658,129 (May 23, 2017).
4. R. Sachs and F. Stanzel, "Interference microscopy for clean air—How optical metrology is improving quality control of fuel injection systems," in *Fringe 2013: 7th International Workshop on Advanced Optical Imaging and Metrology*, W. Osten, ed. (Springer, 2014), pp. 535–538.
5. M. F. Fay and T. Dresel, "Applications of model-based transparent surface films analysis using coherence-scanning interferometry," Opt. Eng. **56**, 111709 (2017).
6. X. Feng, N. Senin, R. Su, and R. Leach, "Optical measurement of surface topographies with transparent coatings," Opt. Laser Eng. **121**, 261–270 (2019).
7. A. Speidel, R. Su, J. Mitchell-Smith, P. Dryburgh, I. Bisterov, D. Pieris, W. Li, R. Patel, M. Clark, and A. T. Clare, "Crystallographic texture can be rapidly determined by electrochemical surface analytics," Acta Mater. **159**, 89–101 (2018).
8. J. DiSciacca, C. Gomez, A. Thompson, S. D. A. Lawes, R. K. Leach, X. Colonna de Lega, and P. de Groot, "True-color 3D surface metrology for additive manufacturing using interference microscopy," in *Proceedings of EUSPEN* (2017), pp. 145–148
9. C. Gomez, R. Su, A. Thompson, J. DiSciacca, S. Lawes, and R. K. Leach, "Optimization of surface measurement for metal additive manufacturing using coherence scanning interferometry," Opt. Eng. **56**, 111714 (2017).
10. D. M. Aikens, A. Roussel, and M. Bray, "Derivation of preliminary specifications for transmitted wavefront and surface roughness for large optics used in inertial confinement fusion," Proc. SPIE **2633**, 350–360 (1995).
11. L. L. Deck and C. Evans, "High performance Fizeau and scanning white-light interferometers for mid-spatial frequency optical testing of free-form optics," Proc. SPIE **5921**, 59210A (2005).
12. M. Davidson, K. Kaufman, and I. Mazor, "The coherence probe microscope," Solid State Technol. **30**, 57–59 (1987).
13. P. de Groot and X. Colonna de Lega, "Interpreting interferometric height measurements using the instrument transfer function," in *Proceedings of the 5th International Workshop on Advanced Optical Metrology* (Springer, 2006), pp. 30–37.
14. P. de Groot, X. Colonna de Lega, R. Su, and R. Leach, "Does interferometry work? A critical look at the foundations of interferometric surface topography measurement," Proc. SPIE **11102**, 111020G (2019).
15. F. Gao, R. K. Leach, J. Petzing, and J. M. Coupland, "Surface measurement errors using commercial scanning white light interferometers," Meas. Sci. Technol. **19**, 015303 (2008).
16. S. Wang, "Coherent phase transfer function degradation due to wave aberrations of a laser Fizeau interferometer," Opt. Eng. **56**, 111711 (2017).
17. ISO, *25178-600: Geometrical Product Specifications (GPS)—Surface Texture: Areal—Part 600: Metrological Characteristics for Areal-topography Measuring Methods* (International Organization for Standardization, 2019).
18. R. K. Leach, C. Giusca, H. Haitjema, C. Evans, and X. Jiang, "Calibration and verification of areal surface texture measuring instruments," CIRP Ann. **64**, 797–813 (2015).
19. C. Gomez, R. Su, P. de Groot, and R. K. Leach, "Noise reduction in coherence scanning interferometry for surface topography measurement," Nanomanuf. Metrol. **3**, 68–76 (2020).
20. J. W. Goodman, *Introduction to Fourier Optics* (W. H. Freeman Macmillan Learning, 2017).
21. M. Pluta, "Image formation in the microscope within the scope of diffraction theory and of Fourier Optics," in *Principles and Basic Properties* (Elsevier, 1988), pp. 287–373.
22. D. G. Voelz, *Computational Fourier Optics: A MATLAB Tutorial* (SPIE, 2011).
23. B. R. Frieden, "Optical transfer of the three-dimensional object," J. Opt. Soc. Am. **57**, 56–66 (1967).
24. M. V. Mantravadi and D. Malacara, "Newton, Fizeau, and Haidinger interferometers," in *Optical Shop Testing*, D. Malacara, ed. (Wiley-Interscience, 2007), pp. 361–394.
25. E. Wolf, "Three-dimensional structure determination of semi-transparent objects from holographic data," Opt. Commun. **1**, 153–156 (1969).
26. J. L. Beverage, R. V. Shack, and M. R. Descour, "Measurement of the three-dimensional microscope point spread function using a Shack–Hartmann wavefront sensor," J. Microsc. **205**, 61–75 (2002).
27. J. M. Coupland and J. Lobera, "Holography, tomography and 3D microscopy as linear filtering operations," Meas. Sci. Technol. **19**, 074012 (2008).
28. R. Su, M. Thomas, M. Liu, J. Drs, Y. Bellouard, C. Pruss, J. Coupland, and R. Leach, "Lens aberration compensation in interference microscopy," Opt. Laser Eng. **128**, 106015 (2020).

29. P. de Groot, X. Colonna de Lega, J. Liesener, and M. Darwin, "Metrology of optically-unresolved features using interferometric surface profiling and RCWA modeling," Opt. Express **16**, 3970–3975 (2008).
30. M. Thomas, R. Su, N. Nikolaev, J. Coupland, and R. Leach, "Modeling of interference microscopy beyond the linear regime," Opt. Eng. **59**, 034110 (2020).
31. W. Xie, "Transfer characteristics of white light interferometers and confocal microscopes," Ph.D. dissertation (University of Kassel, 2017).
32. P. Beckmann and A. Spizzichino, *The Scattering of Electromagnetic Waves from Rough Surfaces* (Artech House, 1987).
33. P. de Groot and X. Colonna de Lega, "Signal modeling for low-coherence height-scanning interference microscopy," Appl. Opt. **43**, 4821–4830 (2004).
34. G. C. Sherman, "Application of the convolution theorem to Rayleigh's integral formulas," J. Opt. Soc. Am. **57**, 546–547 (1967).
35. E. Abbe, "Beiträge zur Theorie des Mikroskops und der mikroskopischen Wahrnehmung," Arch. Mikroskopische Anatomie **9**, 413–418 (1873).
36. L. L. Deck, "Method and apparatus for optimizing the optical performance of interferometers," U.S. patent 10,267,617 (April 23, 2019).
37. D. C. Ghiglia and M. D. Pritt, *Two-Dimensional Phase Unwrapping, Theory, Algorithms, and Software* (Wiley, 1998).
38. H. Schreiber and J. H. Bruning, "Phase shifting interferometry," in *Optical Shop Testing*, D. Malacara, ed. (Wiley, 2006), pp. 547–666.
39. M. Pluta, *Principles and Basic Properties* (Elsevier, 1988).
40. H. H. Hopkins, "Applications of coherence theory in microscopy and interferometry," J. Opt. Soc. Am. **47**, 508–526 (1957).
41. M. Totzeck, "Numerical simulation of high-NA quantitative polarization microscopy and corresponding near-fields," Optik **112**, 399–406 (2001).
42. G. O. Reynolds, J. B. DeVelis, J. George, B. Parrent, and B. J. Thompson, *The New Physical Optics Notebook: Tutorials in Fourier Optics* (SPIE, 1989).
43. P. Lehmann, S. Tereschenko, B. Allendorf, S. Hagemeier, and L. Hüser, "Spectral composition of low-coherence interferograms at high numerical apertures," J. Eur. Opt. Soc. **15**, 5 (2019).
44. D. Maystre, O. M. Mendez, and A. Roger, "A new electromagnetic theory for scattering from shallow rough surfaces," Opt. Acta **30**, 1707–1723 (1983).
45. R. Bracewell, *The Fourier Transform and Its Applications* (McGraw-Hill, 2000), pp. 46–47.
46. G. Schulz, "Über Interferenzen gleicher Dicke und Längenmessung mit Lichtwellen," Ann. Phys. **449**, 177–187 (1954).
47. C. J. R. Sheppard and K. G. Larkin, "Effect of numerical aperture on interference fringe spacing," Appl. Opt. **34**, 4731–4734 (1995).
48. P. de Groot, "Error compensation in phase shifting interferometry," U.S. patent 7,948,637 (May 24, 2011).
49. A. Dubois, J. Selb, L. Vabre, and A.-C. Boccara, "Phase measurements with wide-aperture interferometers," Appl. Opt. **39**, 2326–2331 (2000).
50. G. D. Boreman, *Modulation Transfer Function in Optical and Electro-Optical Systems* (SPIE, 2001).
51. M. De and P. K. Mondal, "Phase and amplitude contrast microscopy in partially coherent light," J. Res. Natl. Bur. Stand., Sect. C **69C**, 199 (1965).
52. Y. Ichioka and T. Suzuki, "Image of a periodic complex object in an optical system under partially coherent illumination," J. Opt. Soc. Am. **66**, 921–932 (1976).
53. I. Abdulhalim, "Spatial and temporal coherence effects in interference microscopy and full-field optical coherence tomography," Ann. Phys. **524**, 787–804 (2012).
54. E. Novak, C. Ai, and J. C. Wyant, "Transfer function characterization of laser Fizeau interferometer for high-spatial-frequency phase measurements," Proc. SPIE **3134**, 114–121 (1997).
55. B. Doerband and J. Hetzler, "Characterizing lateral resolution of interferometers: the height transfer function (HTF)," Proc. SPIE **5878**, 587806 (2005).
56. E. Church, C. Dainty, D. Gale, and P. Takacs, "Comparison of optical and mechanical measurements of surface finish," Proc. SPIE **1531**, 234–250 (1992).
57. A. Fujii, H. Suzuki, and K. Yanagi, "Development of measurement standards for verifying functional performance of surface texture measuring instruments," J. Phys. Conf. Ser. **311**, 012009 (2011).
58. V. G. Badami, J. Liesener, C. J. Evans, and P. de Groot, "Evaluation of the measurement performance of a coherence scanning microscope using roughness specimens," in *Proc. ASPE* (2011), pp. 23–26.